SUPPLEMENTARY INFORMATION

Metal-substrate-supported tungsten-oxide nanoarrays *via* porous-alumina-assisted anodization: From nanocolumns to nanocapsules and nanotubes

Alexander Mozalev,*[a] Maria Bendova,[a] Francesc Gispert-Guirado,[b] Zdenek Pytlicek[a] and Eduard Llobet[b]

[a] CEITEC - Central European Institute of Technology, Brno University of Technology, Technicka 10, 61600 Brno, Czech Republic

[b] MINOS-EMaS, University Rovira i Virgili, Av. Paisos Catalans 26, 43007 Tarragona, Spain

* E-mail: alexander.mozalev@ceitec.vutbr.cz.

S.1. Electrochemical properties

S.1.1. Fitting of the EIS data of the air-annealed sample

The EIS data of the air-annealed sample (Fig. 8b) were best fitted using a circuit containing three R–CPE loops connected in series. The fitted values of effective capacitances (C_1, C_2, and C_3) and parallel resistances (R_1, R_2, and R_3), corresponding to three capacitive layers connected in series, having $R_1 > R_2 > R_3$, are shown as their voltage-dependencies in Fig. S1. Owing to the typical behavior of a space-charge layer formed at a semiconductor–electrolyte interface (*i.e.* linear $1/C^2(V)$, high R, R increasing with voltage), we assign the high-resistance capacitance (C_1 in Fig. S1) to a charge depletion layer formed at the column tops. The other two capacitances and their corresponding resistances (30–60 μF·cm^{-2} and ~10^2–10^4 Ω·cm^2, respectively, when taking into account a 10% column area) fit well with double layers, due to their magnitudes and low voltage dependence of the capacitance.[1]

Additional notes to the fitting:

- R_1 was set to a minimum possible value during fitting, however, due to a short frequency range measured, the R_1 values are less reliable,

- eventually, an $R(RQ)(RQ)$ circuit can be used for fitting of the EIS spectra at voltages >0 V, which results in the same values of R_1 and C_1, but having a bigger fitting error.
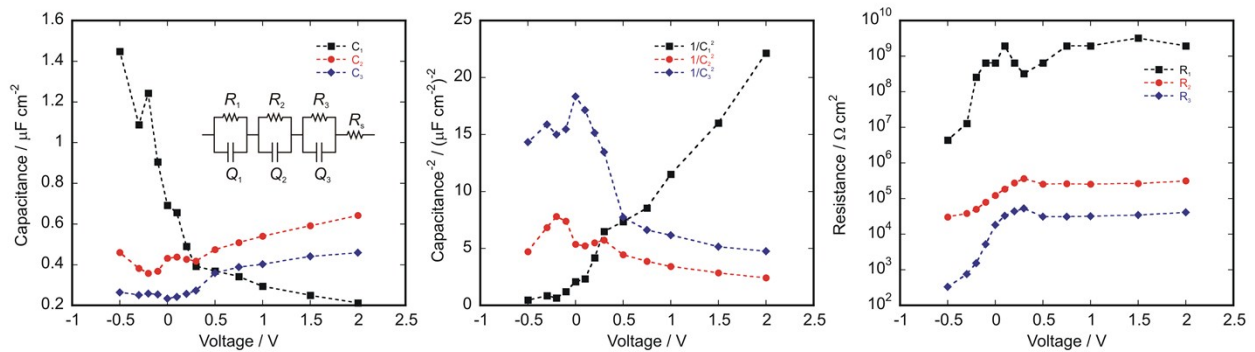

Fig. S1. Dependencies of effective capacitances and parallel resistances on voltage for the air-annealed sample, obtained by fitting of the measured EIS data shown in Fig. 8b using an $R(RQ)(RQ)(RQ)$ circuit.

S 1.2. Fitting of the EIS data of the vacuum-annealed sample

The EIS data of the vacuum-annealed sample (Fig. 8c) were best fitted using a circuit of one R–CPE loop, having an additional CPE in series with the resistance. The fitted values of capacitances (C_0 and C_1) and parallel resistance (R_1), are shown as voltage-dependencies in Fig. S2. The voltage-dependent behavior of parameters C_1 and R_1 fits with a space-charge layer at column tops (linear $1/C^2(V)$ and high R, but R is decreasing with voltage, although an increase is expected; on the other hand, the corresponding exponent of CPE is increasing with voltage from 0.85 to 0.95, in line with the theory). The capacitance C_0 of the $R(RQQ)$ circuit, being in series with R_1, can be related with diffusion processes in the electrolyte (it has a low CPE exponent of 0.3 to 0.8, not shown).

Additionally, several equivalent circuits may be used for fitting of the measured data: $R(RQ)$ is more suitable for voltages below −0.3 V and both $R(RQQ)$ and $R(RQ)(RQ)$ are possible for voltages above −0.3 V, $R(RQQ)$ showing lower fitting errors. The R and C parameters of the main capacitive layer of all circuits are very similar, thus only the parameters of the $R(RQQ)$ fitting are shown in Fig. S2 and are used for Mott-Schottky evaluation.
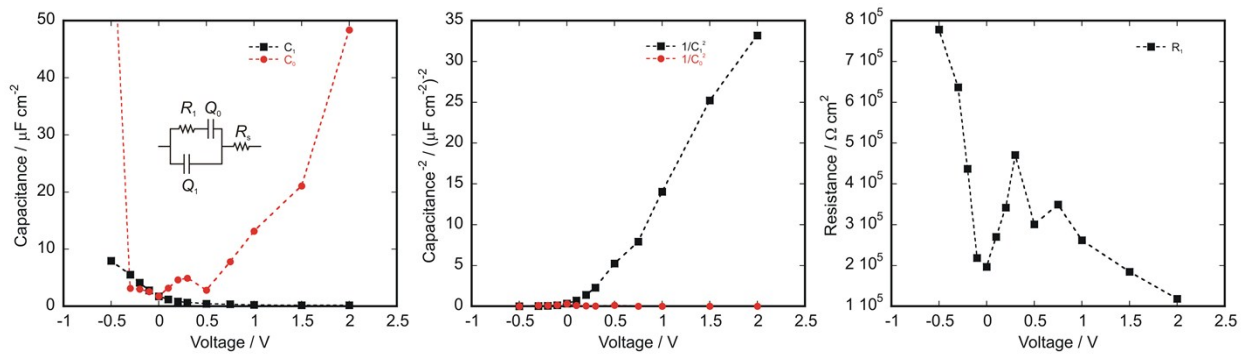

Fig. S2. Dependencies of effective capacitances and parallel resistance on voltage for the vacuum-annealed sample, obtained by fitting of the measured EIS data shown in Fig. 8c using an $R(RQQ)$ circuit.

S.2. XRD analysis and interpretation

S.2.1. Microstructural analysis

The microstructural analysis from the peak broadening was performed with the Double-Voigt Approach[2] for all phases detected (see **Table S1**). According to this approach, in the best case the convolution of up to four functions can be fitted: a Lorentzian and Gaussian functions for the crystallite size effect (β_{LS} and β_{GS}) and Lorentzian and Gaussian (β_{LD} and β_{GD}) functions for the distortion or micro strain effects. However in practice it is difficult to use the four functions simultaneously because they are highly correlated unless the diffractogram covers a wide enough 2θ range. For the most abundant phase, W, the refining was worse if we only considered the term β_{LS}. A quick observation of the diffractograms at high angles showed that the peaks were mainly Gaussians. In fact, an attempt to fit the peaks of W with the β_{LS} failed and was only successful with the β_{GD} component and with a minor contribution of β_{LS}. Both the crystallite size and the mean microstrain, $e_o = \Delta d / d$, can be estimated from the four components of the peak broadening with the well-known expressions.[3]

As is to be expected from a thin layer shape sample, the preferred orientation or texture is an important factor to be corrected for all phases that are deposited. The non-uniform intensity of the Debye rings along the γ angle is apparent. The simplest and easiest model for correcting the texture is the March-Dollase model,[4] which in the TOPAS software allows up to three independent parameters to be fitted for a maximum of two crystallographic directions. In the present case, only one direction for α-Ti and W phases was needed whereas two directions were used for WO_3.

S.2.2 Peak asymmetry

The presence of α-Ti was established from both the asymmetry of the low- and high-angle peaks and the presence of the small peak at $\approx 35°$ 2θ. This small peak matches the 010 reflection for α-Ti as it is shown in Fig. 7a, and it is the only reflection of α-Ti that is alone in this figure. In Fig. 7b and 7c this small peak $\approx 35°$ 2θ is not as clearly seen as in Fig 7a because of the presence of tungsten oxide peaks. However, based on comparison of the diffractograms of the three

samples – as-anodized, vacuum-annealed, and air-annealed, we assume that α-Ti is present in all of them. The 022 reflection of W is also overlapped at high angles by the 022 reflection of α-Ti. We did not include the label of such reflection in Fig. 7 of the main text just for simplicity.

The recorded diffractograms (2θ range and the instrumental resolution) do not allow us to assure the reader on the presence of stacking faults in the tungsten layer. As far as we know, the presence of stacking faults in fcc structures produces a 2θ shift of the reflections as a function of their hkl indexes. In bcc structures, like W is, the effect could be similar but we have not found any precedent in the literature that would clearly mention the asymmetry of W peaks as a consequence of stacking faults.

S.2.3. Crystallite size

The estimated values of the crystallite size (for W and α-Ti) and microstrain (for W) only orientate on the microstructure of all the phases involved. We tried to relate the rough microstructure deduced from the experimental diffractograms with the film preparation procedure, as it is mentioned in the paper. The crystallite size reported for α-Ti assumes that this phase does not have microstrain contribution to the peak broadening. However, for the W phase it was possible to distinguish between the crystallite size and microstrain effects to the peak broadening with the Double-Voigt Approach. We do not intend to make a rigorous study on the microstructure of each phase because of the resolution limit and 2θ range of the recorded diffractograms and because there is no need for a deeper insight into this matter in the frame of this article.

Table 1: Structural data used from the ICSD database, refined cell parameters, crystallite size, microstrain (e_0), preferred orientation correction and calculated wt.% for each phase.

	Space group	ICSD n.	Cell parameters	Microstructure	Preferred orientation	wt.%
The as-anodized sample, not annealed, PAA not dissolved						
W	Im$\bar{3}$m	43421	a: 3.2213(1)	68.4(8) nm e_0: 3.43(5)·10^{-3}	PO$_{011}$: 0.373(3)	95.5
α-Ti	P6$_3$/mmc	44390	a: 2.944(5) c: 4.72(3)	4.3(1)	PO$_{011}$:0.12(6)	4.5
The vacuum-annealed sample, PAA dissolved						
W	Im$\bar{3}$m	43421	a: 3.1972(2)	63.2(1) nm e_0: 2.9(1)·10^{-5}	PO$_{011}$: 0.352 (3)	57.3
α-Ti	P6$_3$/mmc	44390	a: 2.911(6) c: 4.73(3)	6.8(1) nm	PO$_{011}$: 0.11(5)	5.1
WO$_{2.9}$	P2/c	392	a: 11.90(1) b: 3.82(1) c: 61.14(5) β: 99.4(1)	6.8(2) nm	-	37.5
The air-annealed sample, PAA dissolved						
W	Im$\bar{3}$m	434321	a: 3.2004(3)	53.3(2) nm e_0: 3.6(1)·10^{-5}	PO$_{011}$: 0.378(3)	45.2
α-Ti	P6$_3$/mmc	44390	a: 2.906(7) c: 4.73(4)	7.7(2)	PO$_{011}$: 0.12(6)	3.6
WO$_3$	P2$_1$/n	80056	a: 7.33(1) b: 7.556(3) c: 7.718(3) β: 90.3(2)	18(1)	PO$_{100}$: 1.57(4) PO$_{011}$: 0.11(1)	14.2
WO$_{2.9}$	P2/c	392	a: 11.97(1) b: 3.82(1) c: 61.72(2) β: 98.6(2)	5.2(3)		36.9

References

1   A. G. Muñoz, *Electrochim. Acta*, 2007, **52**, 4167–4176.

2   D. Balzar, Voigt-function Model in Diffraction Line-broadening Analysis. In *Defect and Microstructure Analysis by Diffraction*; R. L. Snyder, J. Fiala, H. J. Bunge, Eds.; International Union of Crystallography; Oxford University Press: New York, 1999.

3   A. R. Stokes, A. J. C. Wilson, *Math. Proc. Cambridge Philos. Soc.*, 1942, **38**, 313–322.

4   W. A. Dollase, *J. Appl. Crystallogr.*, 1986, **19**, 267–272.